A finite volume method to solve the Poisson equation with jump conditions and surface charges: Application to electroporation

Thomas Bonnafont, Delphine Bessières, Jean Paillol

A finite volume method to solve the Poisson equation with jump conditions and surface charges: application to electroporation

Thomas Bonnafont[a,*], Delphine Bessieres[b], Jean Paillol[b]

[a] *Lab-STICC UMR CNRS 6285, ENSTA Bretagne, 2 rue François Verny, Brest, 29806, Brest*
[b] *Université de Pau et des Pays de l'Adour, E2S UPPA, SIAME, rue de l'Université, Pau, 64000, France*

Abstract

Efficient numerical schemes for solving the Poisson equation with jump conditions are of great interest for a variety of problems, including the modeling of electroporation phenomena and filamentary discharges. In this paper, we propose a modification to a finite volume scheme, namely the discrete dual finite volume method, in order to account for jump conditions with surface charges, i.e. with a source term. Our numerical tests demonstrate second-order convergence even with highly distorted meshes. We then apply the proposed method to model electroporation phenomena in biological cells by proposing a model that considers the thickness of the cell membrane as a separate domain, which differs from the literature. We show the advantages of the proposed method in this context through numerical experiments.

Keywords:

Poisson equation, Jump conditions, Surface charges, Finite volume method, DDFV, Cell modeling

1. Introduction

Numerical modeling of Poisson equations, in particular with jump conditions, rises in many practical applications, such as cold plasma modeling [1, 2], streamer discharge due to hydro-meteors [3, 4], electroporation [5, 6, 7, 8], or electromagnetic compatibility [9, 10]. In theses cases, many difficulties need to be taken into account. First the mesh can be highly distorted, e.g. moving mesh for cold plasma model [2] or meshing a circular biological cell [11, 8, 12]. Second, in all generality surface charges should be considered in the transition conditions, i.e. a source term in these conditions. Third, the equations can be solved over time [2], thus fast numerical scheme are needed.

In this context, many methods has been developed. For computational efficiency, we focus on low-order ones, such as finite differences [13], P1 finite elements [14, 15] or finite volume [16, 17, 18, 19]. Since a good accuracy for different geometries and highly distorted mesh is needed, finite differences [20, 19] can not be used here. Therefore, we need to choose between finite elements [14, 11, 8, 15] or finite volume methods [19]. Both have good accuracy on distorted mesh and local refinement. Nevertheless, the interface conditions between media can be seen as flux equality, thus a finite volume scheme that preserves the flux consistency conservation seems a good candidate [20, 19]. The

*Corresponding author
Email addresses: thomas.bonnafont@ensta-bretagne.fr (Thomas Bonnafont), delphine.bessieres@univ-pau.fr (Delphine Bessieres), jean.paillol@univ-pau.fr (Jean Paillol)

main drawback of this method is the accuracy of the gradient with a weak convergence of the approximated gradient toward the gradient. This is why the discrete dual finite volume (DDFV) [21, 17, 18, 22] method is preferred here since it overcomes this problem, with a strong convergence of the approximated gradient toward the gradient and better accuracy than usual finite volume schemes.

This latter is a recent finite volume method [21] based on a primal/dual mesh to obtain a diamond mesh. As with other finite volume schemes, we have a local conservative property on each control volume, contrary to the finite element method. On contrary to a two points or four points finite volume scheme, the gradient is approximated in two directions with a strong convergence and without any assumptions on the mesh [17, 18]. Also, with the DDFV method we have a discrete Green relation. Furthermore, jump conditions between medium can be taken into account [23, 17, 24], whereas low-order finite element schemes are not suitable for that.

The error is also at least of the same order as with a FE method [18] of low order. In addition, the method is well suited for related models (Poisson equations with jump conditions, diffusion equations) as mentioned in [18, 20, 19]. Furthermore, mixed boundary conditions are treated through the DDFV scheme. Finally, the scheme is symmetric, has a coercive propriety [18], and is highly parallelizable. All these advantages have thus guided our choice for this computational method, even if two times more discretization points than a conventional finite volumes method are needed.

This article presents an extension to the DDFV computational scheme to account for jump conditions with surface charges, making it applicable to physical applications. The traditional DDFV scheme, which already accounts for discontinuity [23, 17], is modified to incorporate surface charges. Numerical experiments are conducted to validate the proposed method, which shows second-order convergence even with highly distorted meshes. Furthermore, the proposed scheme is applied to model electroporation phenomena in biological cells. To achieve this, we introduce an electrical model of biological cells that considers the thickness of the membrane. This model is based on the metal-dielectric equivalence and the use of Debye's model. The primal/dual scheme of the DDFV method is utilized to compute the potential at the inner and outer surfaces of the membrane without any interpolation. Numerical tests are performed for both stationary and nsPEF-exposed biological cells, showcasing the effectiveness of the proposed method.

The remainder of this article is organized as follows. Section 2 introduces the model, the notations and the computational strategy. Section 3 is devoted numerical experiments on some canonical tests in order to validate the described method. In Section 4, a real-life application is studied. Indeed, we apply the computational strategy to model the electroporation phenomena. Section 5 concludes the paper and gives some perspectives for future works.

2. Description of the computational strategy

2.1. Definition of the problem and notations

Let us consider a domain, denoted by Ω, consisting in n sub-parts, each denoted by $\Omega_i \subset \Omega$, with $i \in [1, n]$, such that $\bigcup_{i=0}^{n} \Omega_i = \Omega$. For these subsets Ω_i, we assume that for $i \neq j$, we have $\Omega_i \cap \Omega_j = \emptyset$. This latter ensures a physical partition of the whole domain. The notation $\partial\Omega$ corresponds to the boundary of the domain Ω. Figure 1 displays a domain Ω with 3 subdomains Ω_1, Ω_2 and Ω_3 that respect the previous condition. The vectors are denoted in bold uppercase, such as $\mathbf{V}$, and in bold lowercase, if normalized, such as $\mathbf{v}$.

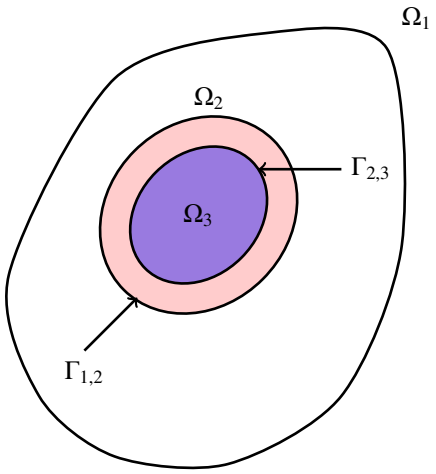

Figure 1: Example of the considered domain Ω with 3 different subdomains Ω_1, Ω_2, and Ω_3. The interfaces between each one are also pictured.

Next, the interfaces between each subdomain are denoted by $\Gamma_{i,j} = \Omega_i \cap \Omega_j$, with i and j corresponding to the indexes of both subdomains considered. The latter are also plotted in the example of Figure 1.

The mathematical formulation of the studied transmission problem is then as follows. We search for $V \in H^1(\Omega)$ solution of

$$\begin{cases} -\nabla \cdot (\varepsilon_i \nabla V_i) &= f_i, & \text{in } \Omega_i \\ \left(\varepsilon_j \nabla V_j - \varepsilon_i \nabla V_i\right) \cdot \mathbf{n}_{i\to j} &= -\sigma_{s,i,j}, & \text{on } \Gamma_{i,j} \\ V_i &= V_j, & \text{on } \Gamma_{i,j} \\ V &= g_k, & \text{on } \partial_{D_k}\Omega \\ \partial_n V &= 0, & \text{on } \partial_N \Omega \end{cases} \tag{1}$$

where ε_i is assumed to differ from media to media, $\sigma_{s,\cdot,\cdot} \in \mathbb{R}$ (this corresponds for example to a surface charge), and $\mathbf{n}_{i\to j}$ is the normalized normal, directed from media i to j, at the interface $\Gamma_{i,j}$. Furthermore, $\partial_{D_k}\Omega$ corresponds to Dirichlet condition, of value $g_k \in \mathbb{R}$, on the boundary of Ω, while $\partial_N\Omega$ are homogeneous Neumann conditions on $\partial\Omega$.

Remark 2.1. In this definition, V corresponds for example to the electrical potential and, in this case, the second and third equation to the interface condition between two different media in terms of electrical potential, where for generality a surface charge is considered here. Thus, we need to solve a Poisson equation with jump conditions. It

should be noted that in many applications such as electroporation (see Section 4) or plasma modeling, this set of equations needs to be solved over time.

2.2. Discretization and notation

In this section, the primal, dual, and diamond meshes are introduced. The last one is the connection between the previous.

The primal mesh $\mathcal{M}$. Let us denote by $\mathcal{M}$ the primal mesh, which corresponds to a non-overlapping partition of the domain Ω. In this article, a quadrangular grid is chosen, with $\mathcal{K}$ that denotes a control volume and $x_{\mathcal{K}}$ its center. The interface between two different control volumes $\mathcal{M}$ and $\mathcal{L}$ is denoted by ν. The set of all these interfaces is denoted by $\mathcal{F}$. The subset of interfaces such that $\mathcal{F} \subset \partial\Omega$ are denoted by $\partial\mathcal{F}$. The latter is divided into two $\partial\mathcal{F}_N$ and $\partial\mathcal{F}_{D_k}$ for the Neumann and Dirichlet boundary conditions, respectively. The number of control volumes in $\mathcal{M}$ is denoted by $N_{\mathcal{M}}$.

Remark 2.2 (Discontinuities and mesh). To define the primal mesh, the method described in [25] is used. Indeed, this allows obtaining a conformal quadrangular grid that follows the physic of the problem. The idea is to solve an optimization problem where the constraints are the physical shape of the subdomains. The initial guess for the optimization is a Cartesian grid of size $N_x \times N_y$. Then, this grid is distorted to follow the limit of each subdomain while keeping a quadrangular grid with the same number of control volumes.

The dual mesh $\mathcal{M}^*$. The second mesh $\mathcal{M}^*$, i.e. the dual mesh, is constructed from the primal mesh by considering the vertices of the primal mesh as the unknowns. On the other hand, the vertices of the dual volume $\mathcal{K}^*$ correspond to the center of the primal mesh. This latter also induces a non-overlapping partition of Ω. The center of the dual control volume $\mathcal{K}^* \in \mathcal{M}^*$, is denoted by $x_{\mathcal{K}^*}$. As for the primal mesh, the interface between two different dual control volumes $\mathcal{M}^*$ and $\mathcal{L}^*$ is denoted by ν^*, while the set of all these interfaces corresponds to $\mathcal{F}^*$. Eventually, the boundary elements of $\mathcal{F}^*$ are denoted by $\partial\mathcal{F}^*$. In $\mathcal{M}^*$ the number of dual control volumes, and unknowns, is denoted by $N_{\mathcal{M}^*}$.

To better explain this construction, Figure 2 displays an example of a quadrangular primal/dual mesh. One can see that the dual mesh $\mathcal{M}^*$ is directly constructed from the primal mesh $\mathcal{M}$ using the vertices as new unknowns and the primal centers as vertices. In this picture, the different notations are also pictured.

The discrete data $V^{\mathcal{T}}$. From now on, an unknown V is searched in $\mathcal{T}$, where $\mathcal{T} = \mathcal{M} \cup \mathcal{M}^*$. Thus, the notation $V^{\mathcal{T}} = (V_{\mathcal{K}\in\mathcal{M}}, V_{\mathcal{K}^*\in\mathcal{M}^*}) \in \mathbb{R}^{\mathcal{T}}$ is used hereafter to refer to the unknown discretized in the primal/dual mesh. Therefore, twice as many unknowns are used with this method than with a usual finite volume scheme. Also, one can note that if the primal mesh is orthogonal then both are uncorrelated and we have two admissible meshes for the usual finite volume method.

Diamond mesh $\mathcal{D}$. Finally, we need to define the diamond mesh, denoted by $\mathcal{D}$, that links $\mathcal{M}$ and $\mathcal{M}^*$ together. A diamond cell $D \in \mathcal{D}$ is constructed from two adjacent control volumes, $\mathcal{K}$ and $\mathcal{L}$, as follows. The diamond D corresponds to the quadrangle defined by $x_{\mathcal{K}} x_{\mathcal{K}^*} x_{\mathcal{L}} x_{\mathcal{L}^*}$, with $x_{\mathcal{K}^*}$ and $x_{\mathcal{L}^*}$ corresponding to the vertices of ν the interface

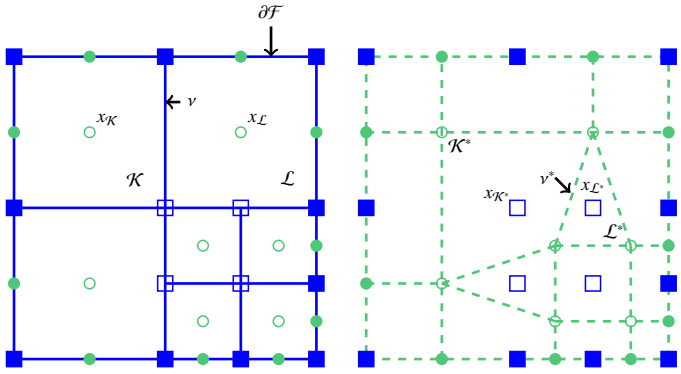

(a) Primal mesh $\mathcal{M}$ (b) Dual mesh $\mathcal{M}^*$

Figure 2: Example of the primal and dual meshes when a quadrangular grid is considered. The circle corresponds to the primal unknowns while the square indicates the dual ones. The filling indicates boundary unknowns. [22]

between $\mathcal{K}$ and $\mathcal{L}$, and also the center of the dual volumes $\mathcal{K}^*$ and $\mathcal{L}^*$. An example of a diamond is pictured in Figure 3. The edge ν^* corresponds to $x_\mathcal{K} x_\mathcal{L}$. We also denote by $\mathbf{N}_\nu$ and $\mathbf{N}_{\nu^*}$ the normal to the two edges ν and ν^*, as picture in the Figure 3. We use lower script $\mathbf{n}_\nu$ (resp. $\mathbf{n}_{\nu^*}$) to denote the normalize vector $\mathbf{N}_\nu$ (resp. $\mathbf{N}_{\nu^*}$).

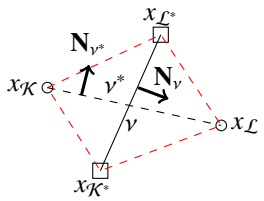

Figure 3: An example of a diamond D of the set of diamonds $\mathcal{D}$.

2.3. Introduction of the discrete operators

In this part, the discrete gradient and divergence in the DDFV framework [21, 18], primal/dual mesh, are introduced. Hereafter, we use the notation $\mathbb{R}^\mathcal{T}$, as mentioned previously, for the set of couples of piece-wise constant real-valued functions on the control volumes $T \in \mathcal{T}$, and $(\mathbb{R}^2)^\mathcal{D}$ the set of vector real-valued piece-wise constant function over the diamond $D \in \mathcal{D}$.

Definition 2.1 (Discrete gradient ∇^D)**.** We define the following application, corresponding to the discrete gradient [17, 18] :

$$\begin{aligned} &\nabla^D V^\mathcal{T} : \mathbb{R}^\mathcal{T} \to (\mathbb{R}^2)^\mathcal{D} \\ &\qquad V \mapsto \mathcal{M}\frac{1}{2|D|}\left(\left(V_{x_\mathcal{L}} - V_{x_\mathcal{K}}\right)\mathbf{N}_\nu + \left(V_{x_{\mathcal{L}^*}} - V_{x_{\mathcal{K}^*}}\right)\mathbf{N}_{\nu^*}\right) \end{aligned} \tag{2}$$

In this definition $|D|$ corresponds to the measure of the diamond D. This operator is the link between the primal/dual mesh and the diamond mesh. A real-valued vector constant over the diamond is obtained here. One can note that this

latter can be obtained as a sum of each mean-value between the two unknowns associated with the two extremities of each segment that constitutes D, see [17].

Definition 2.2 (Discrete divergence)**.** The discrete divergence operator – adjoint operator of the gradient – $\mathrm{div}^{\mathcal{T}} : (\mathbb{R}^2)^{\mathcal{D}} \to \mathbb{R}^{\mathcal{T}}$, linking the diamond mesh to the primal and dual mesh, is defined as [17, 18]

$$\begin{aligned} \forall \mathcal{K} \in \mathcal{M},\ \forall \xi^D \in (\mathbb{R}^2)^{\mathcal{D}}, \quad \mathrm{div}^{\mathcal{T}}_{\mathcal{K}}\left(\xi^D\right) &= \frac{1}{|\mathcal{K}|} \sum_{\nu \in \mathcal{D}_{\mathcal{K}}} \xi^D \cdot \mathbf{N}_{\nu}, \\ \forall \mathcal{K}^* \in \mathcal{M}^*,\ \forall \xi^D \in (\mathbb{R}^2)^{\mathcal{D}}, \quad \mathrm{div}^{\mathcal{T}}_{\mathcal{K}^*}\left(\xi^D\right) &= \frac{1}{|\mathcal{K}^*|} \sum_{\nu^* \in \mathcal{D}_{\mathcal{K}^*}} \xi^D \cdot \mathbf{N}_{\nu^*}, \end{aligned} \tag{3}$$

where $|\mathcal{K}|$ and $|\mathcal{K}^*|$ is the measure of the primal and dual volumes $\mathcal{K}$ and $\mathcal{K}^*$, respectively.

In this definition $\mathcal{D}_{\mathcal{K}}$ (or $\mathcal{D}_{\mathcal{K}^*}$) corresponds to all the diamond where $x_{\mathcal{K}}$ (or $x_{\mathcal{K}^*}$) is a vertex. It can also be seen as the sum of all the flux over all the edges ν (or ν^*) of $\mathcal{K}$ (or $\mathcal{K}^*$), as for a usual finite volume scheme. For example, this corresponds to a sum of 4 elements for each interior primal control volume with a quadrangular grid. The main difference with the usual finite volume schemes is the use of the second mesh, in particular, the gradient is here approximated over two directions, while only the normal one is accounted for in the four-points finite volume method (VF4) for example.

Discrete Green formula. Finally, both operators are linked through a discrete Green formula (as in the continuous domain), as shown in [18]. This latter is given by $\forall V^{\mathcal{T}} \in \mathbb{R}^{\mathcal{T}},\ \forall \xi^D \in (\mathbb{R}^2)^{\mathcal{D}}$:

$$(\xi^D, \nabla^D V^{\mathcal{T}})_{(\mathbb{R}^2)^{\mathcal{D}}} + (\mathrm{div}^{\mathcal{T}} \xi^D, V^{\mathcal{T}})_{\mathbb{R}^{\mathcal{T}}} =< V^{\mathcal{T}}, \xi^D \cdot \mathbf{n} >_{\mathcal{T},\partial\Omega} . \tag{4}$$

In this equation, the three scalar products are defined as follows :

$$\begin{aligned} \forall \xi_1^D, \xi_2^D \in (\mathbb{R}^2)^{\mathcal{D}},\ (\xi_1^D, \xi_2^D)_{(\mathbb{R}^2)^{\mathcal{D}}} &= \int_{\Omega} \xi_1^D \cdot \xi_2^D dx \\ \forall V_1^{\mathcal{T}}, V_2^{\mathcal{T}} \in \mathbb{R}^{\mathcal{T}},\ (V_1^{\mathcal{T}}, V_2^{\mathcal{T}})_{\mathbb{R}^{\mathcal{T}}} &= \frac{1}{2}\left(\sum_{\mathcal{K} \in \mathcal{M}} V_{1,x_{\mathcal{K}}} V_{2,x_{\mathcal{K}}} |\mathcal{K}| + \sum_{\mathcal{K}^* \in \mathcal{M}^*} V_{1,x_{\mathcal{K}^*}} V_{2,x_{\mathcal{K}^*}} |\mathcal{K}^*| \right) \\ \forall \xi^D \in (\mathbb{R}^2)^{\mathcal{D}},\ V^{\mathcal{T}} \in \mathbb{R}^{\mathcal{T}},\ < V^{\mathcal{T}}, \xi^D \cdot \mathbf{n} >_{\mathcal{T},\partial\Omega} &= \int_{\partial\Omega} \tilde{V}^{\mathcal{T}} (\xi^D \cdot \mathbf{n}) ds \end{aligned} \tag{5}$$

In the last equation of (5), $\tilde{V}^{\mathcal{T}}$ denotes the piece-wise affine interpolation of $V^{\mathcal{T}}$ over each control volumes.

Remark 2.3 (Homogeneous Neumann conditions). As for a finite element method, with DDFV homogeneous Neumann conditions are easily taken into account since the right-hand side term of (4) is null on $\partial_N \Omega$.

2.4. Introduction of the discontinuity

In this part, the introduction of a discontinuity, as occurred in the toy problem (1), in the DDFV framework is described. The formalism developed by [17, 26] is used here. We assume that the discontinuities only occur between the primal control volumes, but a constant source term – σ_s – is taken into account in the jump condition, whereas in [17, 26, 24] the interface condition corresponds to flux conservation (with 0 on the right-hand side), only ε is

assumed to be discontinuous. The hypothesis of a discontinuity between the cells of $\mathcal{M}$ is valid here since the mesh is computed in order to follow the physic of the problem, as said in Section 2.2, leading to discontinuities only between the primal control volumes.

To account for the jump condition, the idea is to modify the discrete gradient near the discontinuity using a new unknown [17, 24]. This is performed by dividing the diamond D, pictured in Figure 3, into two half-diamond. Then a new flux is computed to determine the unknown. One can note that the discontinuity is accounted as with a usual finite volume method, as seen with the 1D case in [17].

The half-diamonds τ. First, let us define the two considered half-diamonds $\tau_{\mathcal{K}} = x_{\mathcal{K}} x_{\mathcal{K}^*} x_{\mathcal{L}^*}$ and $\tau_{\mathcal{L}} = x_{\mathcal{L}} x_{\mathcal{K}^*} x_{\mathcal{L}^*}$, from the diamond D. Both are plotted in different colors in Figure 4. The new discrete gradients ∇^{τ_i} are built on the DDFV gradient ∇^D, by enforcing it to be constant on each half-diamond τ_i. To do so, we introduce x_ν at the intersection of ν and ν^*. The new unknown is denoted by δ.

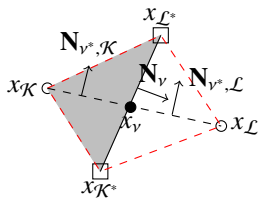

Figure 4: Illustration of the half diamonds in D.

Definition 2.3 (Half-diamond gradient)**.** On the two half-diamonds $\tau_{\mathcal{K}}$ and $\tau_{\mathcal{L}}$, the discrete gradient are expressed as follows [17]

$$\begin{aligned} \nabla^{\tau_{\mathcal{K}}} V^{\mathcal{T}} &= \nabla^D V^{\mathcal{T}} + \frac{\delta}{|\tau_{\mathcal{K}}|} \mathbf{N}_\nu \\ \nabla^{\tau_{\mathcal{L}}} V^{\mathcal{T}} &= \nabla^D V^{\mathcal{T}} - \frac{\delta}{|\tau_{\mathcal{L}}|} \mathbf{N}_\nu \end{aligned} \tag{6}$$

This corresponds to adding the mean value on x_ν to the discrete gradient definition and having the mean value over the half-diamonds that constitutes D equal to the usual DDFV gradient. The new unknown δ is artificial and is computed so as to respect the interface conditions, i.e. the jump conditions.

Computing δ. Here, we differ from [17, 26], since a source term, σ_s, is accounted in the jump condition and the discontinuity only occurs on the primal mesh. For generality, we compute δ for any $\Gamma_{\mathcal{K},\mathcal{L}}$ to respect the second equation of 1

$$(\varepsilon(x^+)\nabla V(x^+) - \varepsilon(x^-)\nabla V(x^-)) \cdot \mathbf{n}_{\mathcal{K}\to\mathcal{L}} = -\sigma_{s,\mathcal{K},\mathcal{L}}. \tag{7}$$

Considering a diamond $D \in \mathcal{D}$ and the two half-diamond $\tau_{\mathcal{K}}$ and $\tau_{\mathcal{L}}$, such that $D = \tau_{\mathcal{K}} \cup \tau_{\mathcal{L}}$, the previous equation can be rewritten as

$$\left(\varepsilon_{\mathcal{L}} \nabla^{\tau_{\mathcal{L}}} V^{\mathcal{T}} - \varepsilon_{\mathcal{K}} \nabla^{\tau_{\mathcal{K}}} V^{\mathcal{T}}\right) \cdot \mathbf{n}_\nu = -\sigma_{s,\mathcal{K},\mathcal{L}}, \tag{8}$$

since $\mathbf{n}_\nu = \mathbf{n}_{\mathcal{K}\to\mathcal{L}}$. Inserting the definition of both half-diamond discrete gradients (6) in (8), we obtain the expression of δ as

$$\delta = \frac{1}{|\nu|}\frac{1}{\frac{\varepsilon_\mathcal{L}}{|\tau_\mathcal{L}|}+\frac{\varepsilon_\mathcal{K}}{|\tau_\mathcal{K}|}}\left((\varepsilon_\mathcal{L}-\varepsilon_\mathcal{K})\,\nabla^D V^\mathcal{T}\cdot\mathbf{n}_\nu+\sigma_{s,\mathcal{K},\mathcal{L}}\right), \tag{9}$$

with $|\nu|$ the measure of the segment ν. Note that if there is no discontinuity, then $\varepsilon_\mathcal{L} = \varepsilon_\mathcal{K}$ and $\sigma_{s,\mathcal{K},\mathcal{L}} = 0$ leading to $\delta = 0$, as expected. With the DDFV scheme, discontinuity is thus easily introduced in the discrete operators by considering half-diamonds.

Remark 2.4. If one wants to also account for discontinuities between dual control volumes, then quarter-diamonds should be considered [17], and a system of 4 equations needs to be solved to compute δ.

2.5. Application to the Poisson equation with jump conditions

Discretization of the toy problem. First, no boundary conditions are accounted for. Thus, in $\mathcal{T}$, the system of equation (1) can be written in the primal and dual mesh as follows

$$\begin{array}{rrcl} \forall\mathcal{K}\in\mathcal{M}, & -\mathrm{div}^\mathcal{T}_\mathcal{K}\left(\varepsilon_\mathcal{K}\nabla^{\tau_\mathcal{K}}V^\mathcal{T}\right) & = & f_\mathcal{K},\\ \forall\mathcal{K}^*\in\mathcal{M}^*, & -\mathrm{div}^\mathcal{T}_{\mathcal{K}^*}\left(\varepsilon_\mathcal{K}\nabla^{\tau_\mathcal{K}}V^\mathcal{T}+\varepsilon_\mathcal{L}\nabla^{\tau_\mathcal{L}}V^\mathcal{T}\right) & = & f_{\mathcal{K}^*}, \end{array} \tag{10}$$

where

$$\begin{aligned} f_\mathcal{K} &= \frac{1}{|\mathcal{K}|}\int_\mathcal{K} f(x)dx,\\ f_{\mathcal{K}^*} &= \frac{1}{|\mathcal{K}^*|}\int_{\mathcal{K}^*} f(x)dx. \end{aligned} \tag{11}$$

Using the definition of both operators, equation (10) is re-casted as finding $V^\mathcal{T}\in\mathbb{R}^\mathcal{T}$ such that

$$\begin{aligned} -\sum_{\nu\in\tau_\mathcal{K}}\varepsilon_\mathcal{K}(\nabla^D V^\mathcal{T}+\frac{\delta}{|\tau_\mathcal{K}|}\mathbf{N}_\nu)\cdot\mathbf{N}_\nu &= |\mathcal{K}|f_\mathcal{K},\\ -\sum_{\nu^*\in\mathcal{D}_{\mathcal{K}^*}}\varepsilon_\mathcal{K}(\nabla^D V^\mathcal{T}+\frac{\delta}{|\tau_\mathcal{K}|}\mathbf{N}_\nu)\cdot\mathbf{N}_{\nu^*,\mathcal{K}}+\varepsilon_\mathcal{L}(\nabla^D V^\mathcal{T}-\frac{\delta}{|\tau_\mathcal{L}|}\mathbf{N}_\nu)\cdot\mathbf{N}_{\nu^*,\mathcal{K}} &= |\mathcal{K}^*|f_{\mathcal{L}^*}. \end{aligned} \tag{12}$$

Remark 2.5. The dissymmetry in the dual equation is due to the jump condition. Indeed, the total flux from $\mathcal{K}^*$ to $\mathcal{L}^*$ corresponds to the sum of the flux going through the segments $x_\mathcal{K}x_\nu$ and $x_\nu x_\mathcal{L}$.

The system of linear equations (12) can then be rewritten as

$$S\,V^\mathcal{T} = M f^\mathcal{T} + D_\delta\sigma_s^\mathcal{T}, \tag{13}$$

where the M – the mass matrix – is a diagonal matrix such that

$$\forall T\in\mathcal{T},\ M[i_T,i_T] = |\mathcal{T}|. \tag{14}$$

This latter contains all the measures of the primal or dual control volumes. The vector $f^\mathcal{T}$ corresponds to the source term expressed in the mesh $\mathcal{T}$. The term $\sigma_s^\mathcal{T}$ corresponds to the surface charge discretized on the primal and dual mesh,

while the diagonal matrix D_δ accounts for the jump condition in the source term as follows

$$D[i_\delta, i_\delta] = \begin{cases} \dfrac{\varepsilon_\mathcal{K} \mathbf{N}_\nu \cdot \mathbf{N}_\nu}{|\nu||\tau_\mathcal{K}|\left(\frac{\varepsilon_\mathcal{L}}{|\tau_\mathcal{L}|} + \frac{\varepsilon_\mathcal{K}}{|\tau_\mathcal{K}|}\right)} & \text{if} \quad 0 \leq i_\delta \leq N_\mathcal{M} - 1 \\ \dfrac{\varepsilon_\mathcal{K} \mathbf{N}_\nu \cdot \mathbf{N}_{\nu^*,\mathcal{K}}}{|\nu||\tau_\mathcal{K}|\left(\frac{\varepsilon_\mathcal{L}}{|\tau_\mathcal{L}|} + \frac{\varepsilon_\mathcal{K}}{|\tau_\mathcal{K}|}\right)} - \dfrac{\varepsilon_\mathcal{L} \mathbf{N}_\nu \cdot \mathbf{N}_{\nu^*,\mathcal{L}}}{|\nu||\tau_\mathcal{L}|\left(\frac{\varepsilon_\mathcal{L}}{|\tau_\mathcal{L}|} + \frac{\varepsilon_\mathcal{K}}{|\tau_\mathcal{K}|}\right)} & \text{if} \quad N_\mathcal{M} \leq i_\delta \leq N_\mathcal{M} + N_{\mathcal{M}^*} \end{cases} \tag{15}$$

Finally, the matrix S – the stiffness matrix – contains all the flux and can be obtained from the elementary matrix s defined as

$$s = \begin{bmatrix} \mathbf{n}_\nu \cdot \mathbf{n}_\nu & -\mathbf{n}_\nu \cdot \mathbf{n}_\nu & \mathbf{n}_{\nu^*} \cdot \mathbf{n}_\nu & -\mathbf{n}_{\nu^*} \cdot \mathbf{n}_\nu \\ -\mathbf{n}_\nu \cdot \mathbf{n}_\nu & \mathbf{n}_\nu \cdot \mathbf{n}_\nu & -\mathbf{n}_{\nu^*} \cdot \mathbf{n}_\nu & \mathbf{n}_{\nu^*} \cdot \mathbf{n}_\nu \\ \mathbf{n}_\nu \cdot \mathbf{n}_{\nu^*} & -\mathbf{n}_\nu \cdot \mathbf{n}_{\nu^*} & \mathbf{n}_{\nu^*} \cdot \mathbf{n}_{\nu^*} & -\mathbf{n}_{\nu^*} \cdot \mathbf{n}_{\nu^*} \\ -\mathbf{n}_\nu \cdot \mathbf{n}_{\nu^*} & \mathbf{n}_\nu \cdot \mathbf{n}_{\nu^*} & -\mathbf{n}_{\nu^*} \cdot \mathbf{n}_{\nu^*} & \mathbf{n}_{\nu^*} \cdot \mathbf{n}_{\nu^*} \end{bmatrix}. \tag{16}$$

Indeed, we have $\mathbf{n}_{\nu^*} = \mathbf{n}_{\nu^*,\mathcal{K}} = \mathbf{n}_{\nu^*,\mathcal{L}}$. Besides, this matrix can be put in the following block form [23]

$$S = \begin{bmatrix} P_p & P_d \\ D_p & D_d \end{bmatrix}, \tag{17}$$

where P_p – D_d – is the matrix containing all the contributions from the primal – dual – points. The two other blocks P_d and D_p correspond to the interactions between the primal and dual points and the dual and primal points, respectively. For each line and column, at most 9 elements are non-null leading to a sparse matrix.

Remark 2.6 (Symmetry). With this view, without discontinuities and $\varepsilon \in \mathbb{R}$ one can easily see that the matrix is symmetric since $P_d = D_p$.

Remark 2.7 (Orthogonal mesh). With an orthogonal mesh, we obtain $P_d = D_d = 0$ leading to two independent usual finite volume schemes.

Accounting for the boundary conditions. Second, we consider the mixed Dirichlet-Neumann boundary conditions of the problem (1). The homogeneous Neumann conditions are implicitly taken into account, as in the finite element method, with the discrete Green relation (4). For the Dirichlet ones, on $\partial_{D_k}\Omega$, the penalty method [27, 28] is applied. Thus, the system of equations is rewritten as searching $V^\mathcal{T} \in \mathbb{R}^\mathcal{T}$ such that

$$\left(S + \epsilon^{-1} D_{\text{pen}}\right) V^\mathcal{T} = M f^\mathcal{T} + D_\delta \sigma_s^\mathcal{T} + \epsilon^{-1} g_D^\mathcal{T}, \tag{18}$$

with ϵ a very low value such that ϵ^{-1} is a very high value, D_{pen} a diagonal matrix with 1 at the index of the Dirichlet boundary conditions, and $g_D^\mathcal{T}$ the vector containing the values of the different Dirichlet conditions at their index.

Proposition 2.1 (Positive definition)**.** *If ε is positive definite, then the resulting matrix of the DDFV scheme is positive definite. Besides, if ε is symmetric, then the matrix is also symmetric.*

Proof. First, let us put the solution to the problem in the following form

$$V = V^g + \phi, \tag{19}$$

such that $V^g(x) = g_k \ \forall x \in \partial_{D_k}\Omega$ and $V^g(x) = 0 \ \forall x \in \mathcal{T}$, and $\phi \in \mathcal{R}^{\mathcal{T}}$ solution of the problem (1) with homogeneous Dirichlet conditions. Besides, we define D the operator, such that

$$D\phi = \mathrm{div}_h^{\mathcal{T}}(\varepsilon_i \nabla^D \phi_i^{\mathcal{T}}), \tag{20}$$

with $h = \mathcal{K}$ or $\mathcal{K}^*$ and i corresponding to the number of a subdomain in Ω.

For the following proof, we also introduce $\psi \in \mathbb{R}^{\mathcal{T}}$ solution of the toy problem with homogeneous Dirichlet condition. Using those definitions, we rewrite the studied problem in the following weak form

$$(D\phi, \psi)_\Omega = \sum_i (\mathrm{div}_h^{\mathcal{T}}(\varepsilon_i \nabla^D \phi_i^{\mathcal{T}}), \psi_i)_{\Omega_i}. \tag{21}$$

We then apply the discrete Green formula to each term of the sum. For a given i, this leads to

$$(\mathrm{div}_h^{\mathcal{T}}(\varepsilon_i \nabla^D \phi_i^{\mathcal{T}}), \psi_i)_{\Omega_i} = -(\varepsilon_i \nabla^D \phi_i^{\mathcal{T}}, \nabla^D \psi_i)_{\Omega_i} + < \varepsilon_i \nabla^D \phi_i^{\mathcal{T}} \cdot \mathbf{n}_{\partial\Omega_i}, \psi_i >_{\partial\Omega_i} . \tag{22}$$

Furthermore, we have $\partial\Omega_i = \Gamma_{i,j} \cup \Gamma_{k,i}$ or $\partial\Omega_i = \partial\Omega \cup \Gamma_{i,j}$. In the second case, this allows rewriting equation (22) as

$$(\mathrm{div}_h^{\mathcal{T}}(\varepsilon_i \nabla^D \phi_i^{\mathcal{T}}), \psi_i)_{\Omega_i} = -(\varepsilon_i \nabla^D \phi_i^{\mathcal{T}}, \nabla^D \psi_i)_{\Omega_i} - < \varepsilon_i \nabla^D \phi_i^{\mathcal{T}} \cdot \mathbf{n}_{\Gamma_{i,j}}, \psi_i >_{\Gamma_{i,j}} + < \varepsilon_i \nabla^D \phi_i^{\mathcal{T}} \cdot \mathbf{n}_{\partial\Omega}, \psi_i >_{\partial\Omega}, \tag{23}$$

where the last term is equal to 0 since on $\partial_N\Omega$ the first part of the scalar product is null, and the second part is null on $\partial_D\Omega$. This leads to

$$(\mathrm{div}_h^{\mathcal{T}}(\varepsilon_i \nabla^D \phi_i^{\mathcal{T}}), \psi_i)_{\Omega_i} = -(\varepsilon_i \nabla^D \phi_i^{\mathcal{T}}, \nabla^D \psi_i)_{\Omega_i} - < \varepsilon_i \nabla^D \phi_i^{\mathcal{T}} \cdot \mathbf{n}_{\Gamma_{i,j}}, \psi_i >_{\Gamma_{i,j}} . \tag{24}$$

In all the other cases, equation (22) can be rewritten as

$$\begin{aligned}(\mathrm{div}_h^{\mathcal{T}}(\varepsilon_i \nabla^D \phi_i^{\mathcal{T}}), \psi_i)_{\Omega_i} = &- (\varepsilon_i \nabla^D \phi_i^{\mathcal{T}}, \nabla^D \psi_i)_{\Omega_i} - < \varepsilon_i \nabla^D \phi_i^{\mathcal{T}} \cdot \mathbf{n}_{\Gamma_{i,j}}, \psi_i >_{\Gamma_{i,j}} \\ &+ < \varepsilon_i \nabla^D \phi_i^{\mathcal{T}} \cdot \mathbf{n}_{\Gamma_{k,i}}, \psi_i >_{\Gamma_{k,i}} .\end{aligned} \tag{25}$$

When summing all those terms to express (21), the sum of different scalar products $\pm < \cdot, \cdot >_{\Gamma_{i,j}}$ introduces the following terms

$$\begin{aligned}< \varepsilon_j \nabla^D \phi_j^{\mathcal{T}} \cdot \mathbf{n}_{\Gamma_{i,j}}, \psi_j >_{\Gamma_{i,j}} - < \varepsilon_i \nabla^D \phi_i^{\mathcal{T}} \cdot \mathbf{n}_{\Gamma_{i,j}}, \psi_i >_{\Gamma_{i,j}} &=< (\varepsilon_j \nabla^D \phi_j^{\mathcal{T}} - \varepsilon_i \nabla^D \phi_i^{\mathcal{T}}) \cdot \mathbf{n}_{\Gamma_{i,j}}, \psi_j - \psi_i >_{\Gamma_{i,j}} \\ &= 0.\end{aligned} \tag{26}$$

Indeed, since ψ is solution to the toy problem, we have $\psi_i = \psi_j$ at each $\Gamma_{i,j}$. Thus, we can conclude that the sum of (21) can be rewritten as

$$(D\phi, \psi)_\Omega = -\sum_i (\varepsilon_i \nabla^D \phi_i^{\mathcal{T}}, \nabla^D \psi_i)_{\Omega_i}. \tag{27}$$

Finally, setting $\phi_i = \psi_i \neq 0$ leads to

$$-(D\phi, \phi)_\Omega > 0, \tag{28}$$

if ε is positive definite. In this case, the matrix of the DDFV scheme is positive definite. Besides, if ε is symmetric the matrix is symmetric. □

Proposition 2.2 (Existence of the solution)**.** *As long as $\partial_D\Omega \neq \emptyset$, then we have the existence and unicity of the solution $V^{\mathcal{T}}$. If $\partial_D\Omega = \emptyset$, then the solution $V^{\mathcal{T}}$ is not unique (obtained up to a constant).*

Proof. The interested reader is referred to [23, 29, 24] □

Remark 2.8. Note that if we are looking for the electrical field **E**, as for plasma applications [2], then in both cases we have the existence and unicity of the solution.

To solve this system, the left-hand side matrix is pre-conditioned using the boomer-AMG preconditioner [30]. Here the preconditioner is necessary for many reasons. First, the resulting matrix S corresponds to the discretization of an unbounded operator, leading to an ill-conditioned resulting matrix. Second, S is not well organized. Indeed, two neighboring points are not necessarily neighbors in the matrix. Third, the mesh is distorted leading to control volumes of different dimensions. Finally, the transmission condition induces a very low eigenvalue in absolute value. The resulting linear system is solved using a parallelized bi-conjugate gradient method of the Hypre library [31].

3. Canonical tests: validation of the method

In this section, we aim at validating the method on two canonical tests. First, a two-layered capacitor is studied, in order to obtain the convergence order of the method when $\sigma_s = 0$. Second, a surface charge is considered, to show that the method works well with $\sigma_s \neq 0$. All the tests are performed on a desktop computer using 4 processors.

3.1. Two-layered capacitor

In this canonical test, we study the following 2D canonical problem in $\Omega = [0,1] \times [0,1]$:

$$\begin{cases} -\nabla \cdot (\varepsilon(x,y)\nabla V) = 0, & \forall (x,y) \in \Omega = \Omega_1 \cup \Omega_2 \\ (\varepsilon(x^+,\cdot)\nabla V(x^+,\cdot) - \varepsilon(x^-,\cdot)\nabla V(x^-,\cdot)) \cdot \mathbf{n}_{1\to 2} = 0, & \forall x \in \Gamma_{1,2} \\ V(x^-) = V(x^+), & \forall x \in \Gamma_{1,2} \\ V(x,\cdot) = 0, & \forall x \in \partial_{D_0}\Omega \\ V(x,\cdot) = 1, & \forall x \in \partial_{D_1}\Omega \\ \partial_n V(\cdot,y) = \partial_n V(\cdot,y) = 0, & \forall y \in \partial_N\Omega \end{cases} \tag{29}$$

In this problem, we define $\Omega_1 = [0, 0.5] \times [0,1]$ and $\Omega_2 = [0.5, 1] \times [0,1]$ as the two different subdomains in Ω. Therefore, $\Gamma_{1,2}$ corresponds to $x = 0.5$, and we have $x^+ = 0.5^+$ and $x^- = 0.5^-$. We assume two Dirichlet conditions on the left and right of the domain, while homogeneous Neumann boundary conditions are taken into account at the upper and lower part of the domain. Finally, the function ε is defined as

$$\varepsilon(x,y) = \begin{cases} \varepsilon_1, \text{if } (x,y) \in \Omega_1 \\ \varepsilon_2, \text{if } (x,y) \in \Omega_2 \end{cases} \tag{30}$$

Here, we set $\varepsilon_1 = 5$ and $\varepsilon_2 = 1$.

This problem corresponds to a two-layered capacitor and the electric potential can be computed analytically. Therefore, it can be used to validate the method and compute its order of convergence. Indeed, the electrical potential $V^{\mathcal{T}}$ is computed – with DDFV – for a decreasing grid size h, i.e. the number of control volumes increases. To compare to the analytical solution V_{ana}, we define the following two errors

$$\text{err}_{L2} = \frac{\|V^{\mathcal{T}} - V_{\text{ana}}\|_2}{\|V_{\text{ana}}\|_2}\,, \text{ and }, \text{err}_{\infty} = \max\left(|V^{\mathcal{T}} - V_{\text{ana}}|\right). \tag{31}$$

Also, to show that the method works well even with distorted meshes, we use a randomly moved Cartesian grid [32]. This latter is constructed as follows. First, a $N_x \times N_y$ Cartesian mesh is built. Second, each point of the grid is moved as

$$\begin{aligned} \forall (i,j) \in [1, N_x] \times [1, N_y],\ x_{ij} &= x_{ij} + \sigma w_x (R_x - 0.5) \\ y_{ij} &= y_{ij} + \sigma w_y (R_y - 0.5), \end{aligned} \tag{32}$$

where $w_x = 1/N_x$ and $w_y = 1/N_y$ are the grid steps along x and y, respectively. In this definition $\sigma \in [0, 1]$ is a distortion parameter, while R_x and R_y are two normalized random variables. Here, we set $\sigma = 0.5$, which induces a highly distorted mesh. Nevertheless, at $x = 0.5$, where the discontinuity occurs, the mesh is not moved in order to respect the physical problem and to ensure the jump condition occurs only between primal control volumes. An example of the obtained mesh for $N_x = N_y = 10$ is given in Figure 5. The primal unknowns are pictured in green.

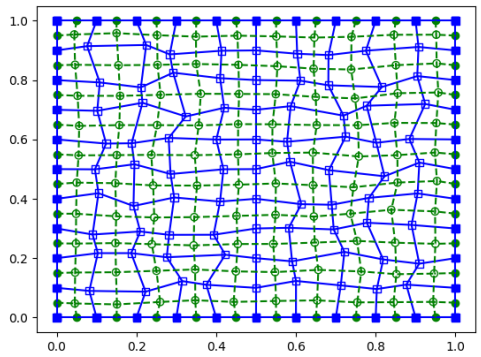

Figure 5: Example of a randomly distorted Cartesian grid for $N_x = N_y = 10$. The green points correspond to the center of each control volume, i.e. the primal unknowns.

In Figure 6, we plot in (a) the two errors with respect to the grid size in a Log/Log scale and the computational efficiency in (b). We also plot the line with a slope of 2 in Figure 6 (a), corresponding to the expecting order [18] when no discontinuity is accounted for.

As expected, the order of 2 is obtained for the method for both the L^2 and the L^∞ norm, even on a very distorted mesh. Besides, the error is very low (below 10^{-11}). Therefore, the method is validated when accounting for a discontinuity. Finally, as can be anticipated the computational cost increase with the accuracy, but is still below 0.4 s for 10221 unknowns.

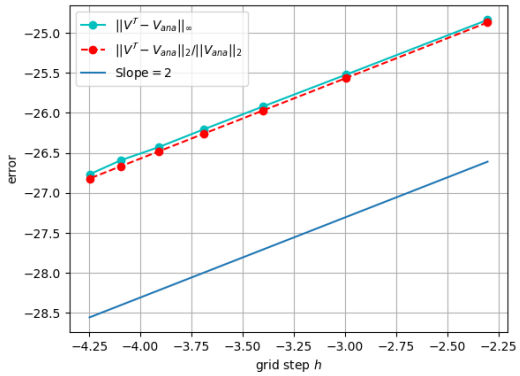

(a) Evolution in a Log/Log scale of the relative L^2 and L^∞ error with respect to the mesh refinement. The slope of 2, expected order, is also pictured for comparison.

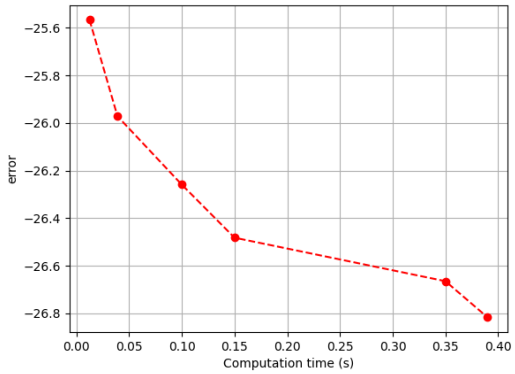

(b) Computational cost of the DDFV method with respect to the accuracy in L^2 norm.

Figure 6: Numerical validation of the DDFV scheme.

3.2. Two-layered capacitor with surface charges

In this second canonical test, the goal is to introduce a surface charge and show that the method works well. Thus, we propose to study the following problem in $\Omega = [0,1] \times [0,1]$

$$\begin{cases} -\nabla \cdot (\varepsilon(x,y)\nabla V) = 0, & \forall (x,y) \in \Omega = \Omega_1 \cup \Omega_2 \\ (\varepsilon(x^+,\cdot)\nabla V(x^+,\cdot) - \varepsilon(x^-,\cdot)\nabla V(x^-,\cdot)) \cdot \mathbf{n}_{1\to 2} = \sigma_{s,1,2}, & \forall x \in \Gamma_{1,2} \\ V(x^-) = V(x^+), & \forall x \in \Gamma_{1,2} \\ V(x,\cdot) = 0, & \forall x \in \partial_{D_0}\Omega \\ \partial_n V(\cdot,y) = \partial_n V(\cdot,y) = 0, & \forall y \in \partial_N \Omega \end{cases} \tag{33}$$

This corresponds to the same problem as before, except that here we account for a surface charge between the two media with $\sigma_{s,1,2} = 8$. Besides, we account for two homogeneous Dirichlet conditions on the right and left side of the domain here. The other parameters remain the same, in particular, ε is still piece-wise constant following (30). In this context, an analytical solution V_{ana} can be computed and as for the previous numerical experiment, the L2-error and the order of the method can be computed by comparison, with

$$\text{err}_{L2} = \frac{\|V^{\mathcal{T}} - V_{\text{ana}}\|_2}{\|V_{\text{ana}}\|_2}, \tag{34}$$

where $V^{\mathcal{T}}$ corresponds to the approximated solution computed with the DDFV method. As before, the computations are performed on a Cartesian grid with an increasing number of control volumes, i.e. a decreasing mesh step h. Here, the results are obtained both on the distorted, with the same method [32] with $\sigma = 0.25$, and the non-distorted grid for comparison.

In Figure 7 (a) and (b), we plot the evolution of the L^2-error with respect to the grid size for the non-distorted and distorted mesh, respectively. We also plot a line with a slope of 2 for comparison.

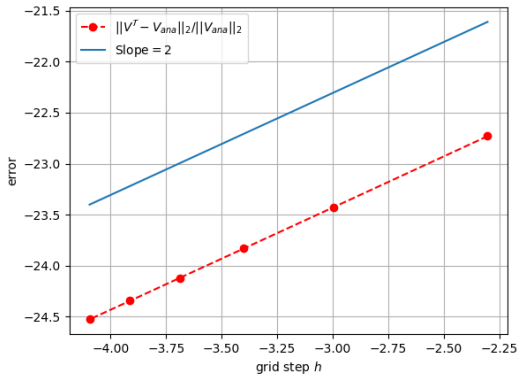

(a) Not distorted mesh.

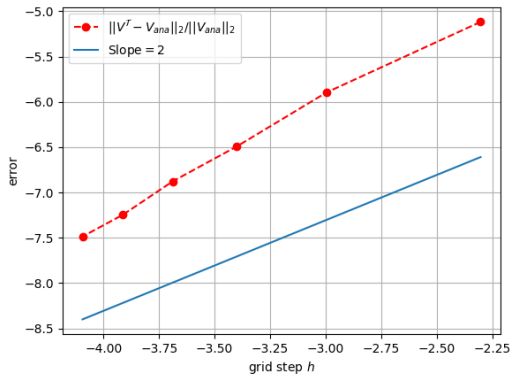

(b) Randomly distorted mesh.

Figure 7: Evolution in a Log/Log scale of the L^2 error with respect to the mesh refinement. The slope of 2 is also pictured for comparison.

First of all, in both cases, the method converges with h decreasing, as expected, with an order of 2 in the L^2-norm. Nevertheless, with a non-distorted mesh, the error is below 10^{-10}, while on the randomly distorted mesh, it is below 10^{-2}. This seems reasonable since the mesh is distorted with a random factor $\sigma = 0.25$, which is high. Besides, even if the mesh at $x = 0.5$ is not moved, the dual one is moved, which can also explain the difference here. In conclusion, when accounting for a surface charge, the DDFV scheme works well, even if the error is higher than when only a discontinuity on ε occurs.

4. Application to the electroporation phenomena

Electroporation is a phenomenon that appears when a sufficiently high electrical field is applied to a biological cell. When this latter condition is fulfilled, the permeability of the membrane can be modified allowing molecules (such as drugs or genes) to enter the cytoplasm. This latter is widely used for clinical applications such as tumor treatment [33, 34], gene therapy [35, 36, 37] or drug delivery [38].

In order to adapt the electric field, it is necessary to accurately describe the cell response to the electrical field, i.e. to model the trans-membrane voltage. Many experimental studies have been carried out [39, 40, 41], while computational schemes mostly rely of the transport lattice method [42, 43, 44], finite element methods [45, 7, 8, 46], or the use of COMSOL [47, 48, 12, 49]. In those cases, the cell membrane is commonly described as a thin interface and replaced by an equivalent resistance and capacitance. Interpolations are then performed to compute the trans-membrane voltage, i.e. difference of potential between the inner and outer surfaces of the membrane.

In this part, we apply DDFV framework to model the electroporation phenomenon. First, we develop a cell electrical model based on the metal-dielectric equivalence that includes the membrane as a whole domain. Indeed, the dual mesh allows for a rigorous treat the effect of the membrane with a low-order method. In addition, the use of the primal/dual mesh allows for direct computation of the potential at the inner and outer surfaces of the membrane.

Furthermore, this example shows a real-life application of the method, where fast and precise results are needed.

4.1. Electrical model for a single cell

Single shell model. In the following work, the single shell model of the 2D cell is studied. This latter is assumed to be spherical, leading to a 2D axisymmetric model. An example of the studied model is pictured in Figure 8.

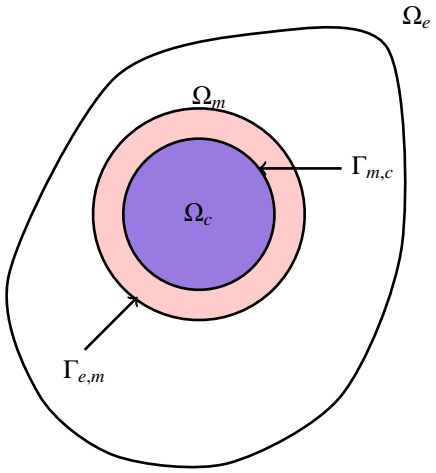

Figure 8: Single shell-model of the cell.

Its corresponds to a domain Ω composed of three subdomains: the exterior media Ω_e, the cytoplasm Ω_c, and the membrane Ω_m, with $\Omega = \Omega_e \cup \Omega_m \cup \Omega_c$ and $\Omega_e \cap \Omega_m \cap \Omega_c = \emptyset$. For each domain, we denote by ε_i and σ_i their permittivity and conductivity, with corresponding to either e, m, or c. Furthermore, the membrane conductivity depends on time if electroporation occurs [47]. We denote by d_m the membrane thickness and by d_c the cytoplasm radius. It should be noted that in comparison to the cell radius $R_d = d_m + d_c$, the membrane is very thin $d_m \ll R_d$ [50, 51, 52, 40]. Note that here the membrane is described as a media, differing from [8]. Magnitudes for the different parameters can be found in [50, 40, 53, 54, 48]. Solving the generalized Poisson equation with jump conditions by a finite volume method. Besides, the cell's media are dispersive and depend on the frequency [55, 56, 54]. In the context of electroporation, we aim at computing the trans-membrane voltage $U_m = V_{\text{outer}} - V_{\text{inner}}$, corresponding to the difference of potential between the inner and outer surfaces of the membrane, and the density of pores N.

Electrical model of a single cell. In the context of electroporation, one can focus on the electro-quasi static problem since the magnetic field magnitude is negligible, as shown in [11]. Thus, we study the electrical induction $\mathbf{D}$, and the electrical field $\mathbf{E}$. In each media Ω_i with $i \in \{e, m, c\}$, both are related through

$$\mathbf{D}_i = \varepsilon_0 \mathbf{E}_i + \mathbf{P}_{i,\text{lin}} + \mathbf{P}_{i,\text{diel}} + \mathbf{P}_{i,\text{disp}}, \quad \text{in } \Omega_i, \tag{35}$$

with ε_0 the free-space permittivity, and $\mathbf{P}_{i,\text{lin}}$, $\mathbf{P}_{i,\text{diel}}$ and $\mathbf{P}_{i,\text{disp}}$ the polarization due to the linear, dielectric and dispersive species in each media, respectively. Furthermore, from the Maxwell-Gauss relation without charge in the domain and

the transition condition between media with no surface charges [54], we have

$$\begin{aligned} \nabla \cdot (\mathbf{D}_i) &= 0, \text{ in } \Omega_i \\ (\mathbf{D}_m - \mathbf{D}_e) \cdot \mathbf{n}_{e\to m} &= 0, \\ (\mathbf{D}_c - \mathbf{D}_m) \cdot \mathbf{n}_{m\to c} &= 0, \end{aligned} \tag{36}$$

where $\mathbf{n}_{i\to j}$ corresponds to the normal oriented from media i to j.

Then, in order to obtain equations in terms of the electrical field or potential, we use the relations that link the polarisation $\mathbf{P}$ to the electrical field $\mathbf{E}$. For each species, this leads in each media Ω_i to

$$\begin{aligned} \mathbf{P}_{i,\text{lin}} &= \varepsilon_0 \left(\varepsilon_{i,r} - 1\right) \mathbf{E}_i, \\ \frac{\partial \mathbf{P}_{i,\text{diel}}}{\partial t} &= \sigma_i \mathbf{E}_i, \\ \tau_i \frac{\partial \mathbf{P}_{i,\text{disp}}}{\partial t} + \mathbf{P}_{i,\text{disp}} &= \varepsilon_0 \left(\varepsilon_{i,r} - \varepsilon_{i,\infty}\right) \mathbf{E}_i. \end{aligned} \tag{37}$$

The second and third equations in (37) are obtained using the metal-dielectric equivalence and a first-order Debye model [57, 58], respectively. In the Debye model τ_i corresponds to the relaxation time, $\varepsilon_{i,r}$ to the static permittivity, and $\varepsilon_{i,\infty}$ to the high-frequency permittivity of the media considered [47, 48]. For better readability, no dispersive species are assumed at first. They are included later on. Thus, by applying a time derivative to the equations (36), and using $\mathbf{E} = -\nabla V$, we obtain the following model

$$\begin{cases} -\nabla \cdot \left(\varepsilon_0 \varepsilon_{i,r} \dfrac{\partial \nabla V_i}{\partial t} + \sigma_i \nabla V_i \right) = 0 & \text{in } \Omega_i \\ (\varepsilon_0 \varepsilon_{m,r} \dfrac{\partial \nabla V_m}{\partial t} + \sigma_m \nabla V_m - \varepsilon_0 \varepsilon_{e,r} \dfrac{\partial \nabla V_e}{\partial t} + \sigma_e \nabla V_e) \cdot \mathbf{n}_{e\to m} = 0 & \text{on } \Gamma_{e,m} \\ V_m = V_e & \text{on } \Gamma_{e,m} \\ (\varepsilon_0 \varepsilon_{c,r} \dfrac{\partial \nabla V_c}{\partial t} + \sigma_c \nabla V_c - \varepsilon_0 \varepsilon_{m,r} \dfrac{\partial \nabla V_m}{\partial t} + \sigma_m \nabla V_m) \cdot \mathbf{n}_{m\to c} = 0 & \text{on } \Gamma_{m,c} \\ V_c = V_m & \text{on } \Gamma_{m,c} \\ V = V^+, & \text{on } \partial_{D_+}\Omega \\ V = V^-, & \text{on } \partial_{D_-}\Omega \\ \partial_n V = 0, & \text{on } \partial_N \Omega \end{cases} \tag{38}$$

Indeed, the cell shape is assumed to not change over time, thus the normal $\mathbf{n}_{i\to j}$ does not depend on time. The first equation of the model (38), i.e. the Poisson one, is of course equivalent to the one derived in [54, 11, 8], as expected. Nevertheless, we depart from [11, 8] since we do not use the conductance and capacitance model of the cell and account for the thickness of the membrane, and from [54] since we consider the time-domain equation. In this model, $\partial_{D_+}\Omega$ and $\partial_{D_-}\Omega$ correspond to two electrodes that model for example a nano-second Pulsed Electrical Field (nsPEF). The same calculations can be performed to add the dispersive effect, adding more terms to the considered equations.

The electroporation equations. We also need to take into account the non-linear effects due to the electroporation process. Indeed, the formation and expansion of pores in the cell membrane must be accounted for. For nsPEF, short

duration pulse, an asymptotic model, assuming pores do not expand after creation, that defines the pore density, is widely used [47, 48]

$$\frac{dN}{dt} = \alpha \exp\left(\frac{U_m^2}{V_{ep}^2}\right)\left(1 - \frac{N(t)}{N_0}\exp\left(-q\frac{U_m^2}{V_{ep}^2}\right)\right), \tag{39}$$

where V_{ep} the characteristic voltage of electroporation, N_0 corresponds to the equilibrium pore density at $U_m = 0$ V, and α and q two constants. Also, when the pore density increases the membrane conductivity σ_m decreases. This phenomenon is described through the following equation [59]

$$\sigma_m(t) = \sigma_{m_0} + N(t)\sigma_p \pi r_p^2 K, \tag{40}$$

with σ_p the conductivity of the medium inside the pores, r_p the pore radius, assumed to be constant $r_p = 0.8$ nm [60, 51], and K given by

$$K = \frac{\exp(u_m) - 1}{\frac{w_0\exp(w_0-\eta u_m)-\eta u_m}{w_0-\eta u_m}\exp(u_m) - \frac{w_0\exp(w_0+\eta u_m)+\eta u_m}{w_0+\eta u_m}}. \tag{41}$$

In equation (41), we have w_0 the energy barrier inside a pore, η the relative entrance length of pores, and $u_m = \frac{q_e}{kT}U_m$ the non-dimensional trans-membrane voltage, with q_e the electric charge of an electron, T the temperature and k the Boltzmann constant. Magnitudes for all these parameters can be found in [47, 12]. Note that other models [45, 7, 13] could be used, but the main point here is to show a real-life application of the proposed numerical scheme, thus we focus on the model used in recent articles [48, 61, 12], and compare our results to the ones they obtained.

4.2. Time discretization of the model

Discretization of (38). The model obtained in the previous section is discretized over time with a step Δt using a forward Euler's method. This leads, when assuming no dispersive effects, to

$$\begin{cases}
-\nabla\cdot\left((\varepsilon_0\varepsilon_{i,r} + \Delta t\sigma_i^{n-1})\nabla V_i^n\right) &=& -\nabla\cdot\left(\varepsilon_0\varepsilon_{i,r}\nabla V_i^{n-1}\right) & \text{in } \Omega_i \\
((\varepsilon_0\varepsilon_m + \Delta t\sigma_m^{n-1})\nabla V_m^n - (\varepsilon_0\varepsilon_e + \Delta t\sigma_e)\nabla V_e^n)\cdot\mathbf{n}_{e\to m} &=& -\sigma_{s,\text{out}}^{n-1} & \text{on } \Gamma_{e,m} \\
V_m^n &=& V_e^n & \text{on } \Gamma_{e,m} \\
((\varepsilon_0\varepsilon_c + \Delta t\sigma_c)\nabla V_c^n - (\varepsilon_0\varepsilon_m + \Delta t\sigma_m^{n-1})\nabla V_m^n)\cdot\mathbf{n}_{m\to c} &=& -\sigma_{s,\text{in}}^{n-1} & \text{on } \Gamma_{m,c} \\
V_c^n &=& V_m^n & \text{on } \Gamma_{m,c} \\
V &=& V^+, & \text{on } \partial_{D_u}\Omega \\
V &=& V^-, & \text{on } \partial_{D_0}\Omega \\
\partial_n V &=& 0, & \text{on } \partial_N\Omega
\end{cases} \tag{42}$$

In this set of equations, both $\sigma_{s,\text{out}}$ and $\sigma_{s,\text{in}}$ correspond to the computed surface charges at the outer and inner surfaces of the cell, respectively. They are given by

$$\begin{aligned}
\sigma_{s,out} &= \left(\varepsilon_0\varepsilon_e\nabla V_e^{n-1} - \varepsilon_0\varepsilon_m\nabla V_m^{n-1}\right)\cdot\mathbf{n}_{e\to m} \\
\sigma_{s,in} &= \left(\varepsilon_0\varepsilon_m\nabla V_m^{n-1} - \varepsilon_0\varepsilon_c\nabla V_c^{n-1}\right)\cdot\mathbf{n}_{m\to c}
\end{aligned} \tag{43}$$

In (42), the first equation is a Poisson equation for the electric potential V with a source term depending on the last iteration over time. It should be noted that time sampling is quite important here. Indeed, since $\varepsilon_0 = 8.85 \times 10^{-12}$ F/m, and ε_r and σ are of order 10^1 and 10^{-1}, a time step too large would only include the effect of the conductivity. Considering dispersive media only add terms to the model. Taking into account the constitutive relation of $\mathbf{D}_i$ in the model introduces a second term on the right side of the boundary relations. This latter is negligible when no dispersive species are accounted for [54]. In the other case, this corresponds to electric charges being tied up at the inner and outer surfaces of the membrane, leading to a surface charge. Therefore, the obtained model (42) is of the same form as the toy problem (1), and can thus be efficiently solved using the described DDFV scheme. Furthermore, the source term can be computed by multiplying by a pre-computed stiffness matrix S', of the same form as for the DDFV scheme, and with the computed solution V at the time step considered. The same goes for $\sigma_{s,\cdot}$, since they correspond to flux. Thus, the computational model is self-consistent.

Discretization of the electroporation equations. Furthermore, at each time step the trans-membrane voltage is defined as

$$U_m^n = V^n(R_d) - V^n(R_d - d_m), \tag{44}$$

and corresponds to the difference of electric potential at the outer and inner surfaces of the membrane, as in [47, 48, 12]. Thus the values of the potential at the inner and outer surfaces of the cell are very important.

Finally, the pore density equation (39) is discretized using an implicit scheme as follows

$$\frac{N^n - N^{n-1}}{\Delta t} = \alpha \exp\left(\frac{(U_m^n)^2}{V_{ep}^2}\right)\left(1 - \frac{N^n}{N_0}\exp\left(-q(\frac{(U_m^n)^2}{V_{ep}^2}\right)\right). \tag{45}$$

Thus, at each time step, the transmembrane voltage is computed, then the density of pores N is obtained and the conductivity is modified to obtain σ_m^n. Besides, the time step Δt is also restricted by the mean evolution of N over t. Using the differential equation of the pore density (39), we can approximate its time constant as

$$\tau \simeq \frac{N_0}{\alpha}\exp\left((q-1)\frac{U_m^2}{V_{ep}^2}\right). \tag{46}$$

Given the magnitude in [47], we have

$$\tau \simeq \frac{N_0}{\alpha} \simeq 10^{-3}. \tag{47}$$

Therefore, the time sampling for a precise numerical scheme is strengthened to be of the order of ε_0.

4.3. Numerical experiments

In this part, the derived DDFV scheme, see section 2.5, is used to solve the proposed model of the cell in two cases. First, to show that the method works well, the stationary case is studied. Second, a canonical electroporation test is studied, corresponding to the application of interest here.

4.3.1. Stationary case

Now, the method is applied to the academic study of the spherical cell. The numerical setup is described in Figure 9. The domain, denoted by Ω is a rectangle. The Cartesian coordinates system (x, y) is used in this context. The domain is of size 1 μm in x and 2 μm in y. The cell is placed at $x_c = 0.5$ μm and $y_c = 0$ μm, such that it is at the center of the computational domain. Therefore, we can only study the upper sub-domain $\Omega_s = [0, 1]\times[0, 0.5]$ μm^2, with half the cell. The lower half can be obtained through axial symmetry. The cell radius is $R_d = 0.2$ μm, while the membrane thickness is $d_m = 0.0008$ μm. The thickness-to-radius ratio is of the order of magnitude of the real cell data [56]. For this test, we consider the static case and assume no conductivity. The electrical parameters are as follows: $\varepsilon_e = \varepsilon_c = 80$, and $\varepsilon_m = 2$, for the exterior and cytoplasm domain and for the membrane, respectively. We set $V^+ = 1$ V and $V^- = -1$ V at the left and ride side of the domain, respectively. We consider homogeneous Neumann conditions on the upper and lower boundaries of the domain.

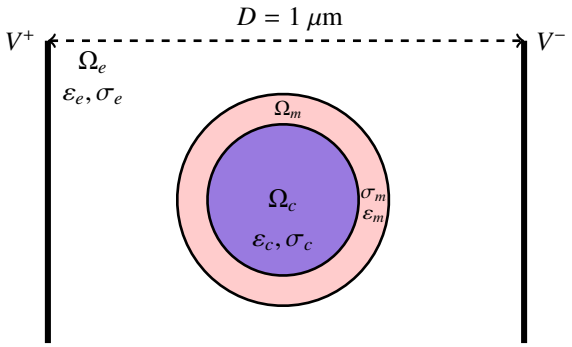

Figure 9: Numerical setup for the single spherical cell.

In this context, a conformal and structured mesh is obtained using the method of Hyman *et al.* [25]. To do so the points on the inner and outer surfaces of the membrane are defined as constraints, and a Cartesian quadrangular grid is optimized to follow those constraints. The obtained mesh with the control volumes centers is plotted in Figure 10. The mesh, which is the primal, is pictured in blue while the primal cell centers are in green. We also add zoom in different parts of the mesh: the cell and the upper part of the membrane. Note that, in this model, the membrane is discretized with one cell. Thus, since the dual cell centers correspond to the vertex of the blue quadrangles, the potential at the inner and outer surfaces of the membrane are precisely computed here, without any interpolation, to then obtain the trans-membrane voltage U_m. This adds an advantage to the use of the DDFV scheme in this context. The potential inside the membrane is also computed through the primal cell centers. Also, the primal vertices are on the discontinuity, so as to have the jump conditions only between primal centers, as assumed in section 2.4.

The DDFV scheme introduced in 2.5 is then applied to the cell model 4.2, described with equations (42), in the stationary case. Since the electrical parameters in the cell and in the exterior domain are the same, we expect the same variations for V in both sub-domains. In the membrane, we expect a great decrease in the electrical potential. The latter is thus plotted on the overall domain in Figure 11 (a). Then, a zoom on the cell potential is represented in Figure 11 (b).

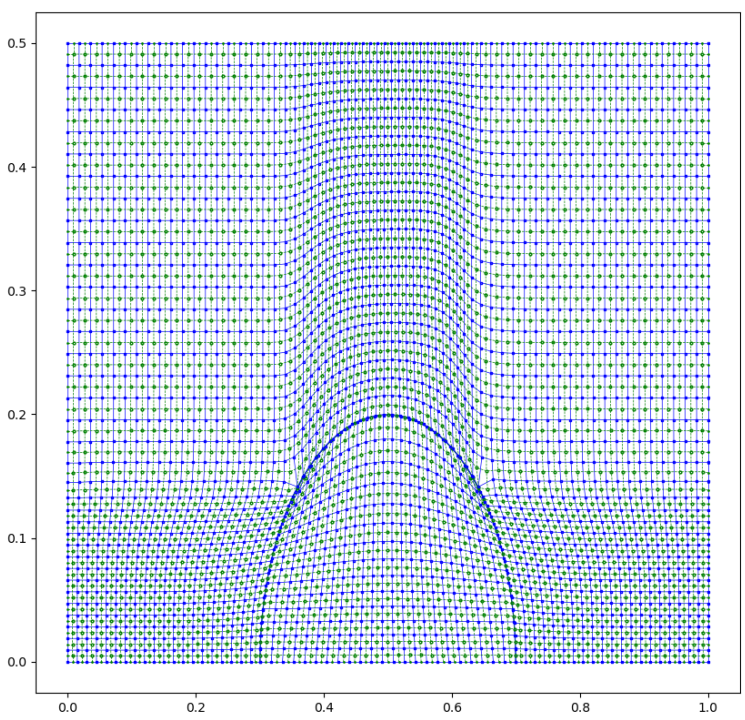

(a) Global mesh.

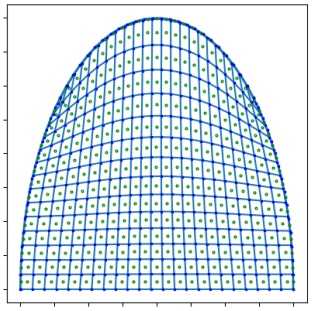

(b) Zoom on the cell.

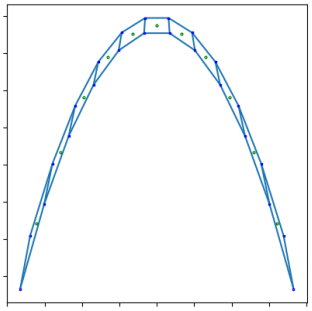

(c) Zoom on the membrane.

Figure 10: Conformal quadrangular mesh for the cell model.

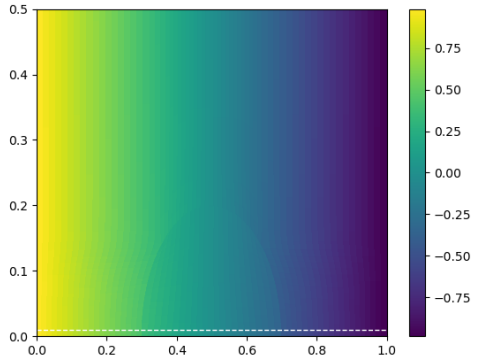

(a) Electrical potential on the whole domain

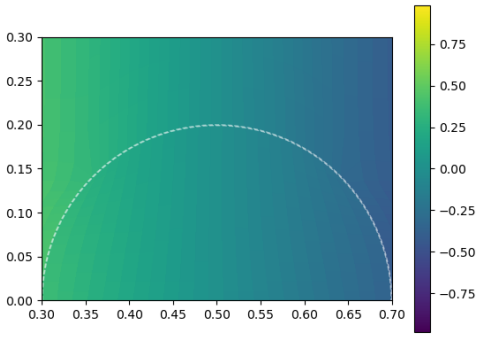

(b) Electrical potential in the cell

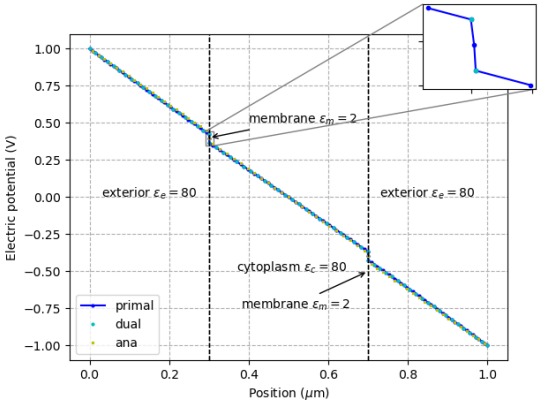

(c) Potential on an equatorial cut along the cell

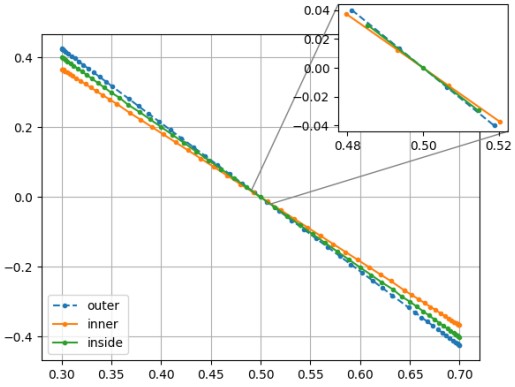

(d) Potential in the membrane

Figure 11: Electric potential V computed with DDFV for the stationary cell model.

The white dotted line corresponds to the following zoom. The potential along an equatorial cut, the white dotted line plotted in (a), through the cell is also pictured in Figure 11 (c). On this figure, we also plot an analytical calculation of the potential in yellow. Finally, the electric potential in the membrane, and at the inner and outer surface of this latter, is plotted in Figure 11 (d). In Figure 11 (c) and (d), a zoom on different areas is also proposed.

First, Figure 11 (a) shows that the potential is decreasing from 1 to -1 V. Also, with the zoom on the cell in Figure 11 (b), we can see that no discontinuity appears on and near the cell. This is highlighted in Figure 11 (d), where we observe no discontinuity in the membrane potential. One can also note, that the potential is equal to 0 at $x = 0.5$ for the potential in the membrane, and at its inner and outer surface, as expected since the electric field is tangential at this point. Second, we observe in Figure 11 (c) that the potential decrease with the same slope in the exterior media and in the cell, as expected. Indeed, in both mediums, the permittivity ε_e and ε_c are the same. Also, with $\varepsilon_m \ll \varepsilon_e = \varepsilon_c$, the potential V is rapidly decreasing in the membrane. Nevertheless, no discontinuity due to the computational scheme appears. Furthermore, these results are in line with the one described and obtained in [56] and correspond the analytical

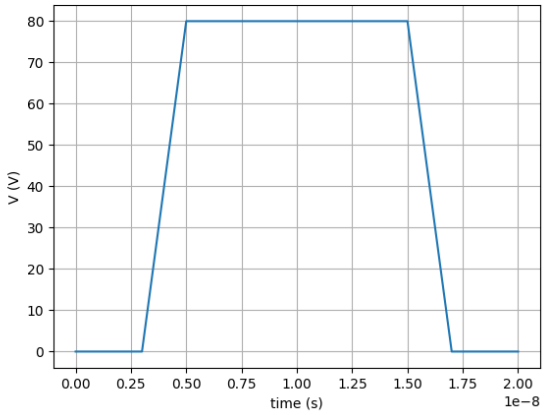

Figure 12: Applied trapezoidal rise-time pulsed voltage waveform used in this study.

calculation. Moreover, note that the two cyan points corresponding to the dual vertex on the membrane allow us to directly compute the potential at the inner and outer surfaces of the membrane. This test shows that the method works well in the context of electric cell modeling.

4.3.2. Cell exposed to a nsPEF

We now study the cell response to a nsPEF. For the cell parameters, we use the one given in [61] while the mesh remains the same. The main difference with the previous test is that the conductivity σ of each media is taken into account, and is varying in the membrane at each time step with the pore density. For each media the electromagnetic parameters are as follows: $\varepsilon_e = \varepsilon_c = 67$, $\varepsilon_m = 5$, and $\sigma_e = \sigma_c = 0.55$ S/m, and $\sigma_{m_0} = 1.1\times10^{-7}$ S/m for the permittivity and the conductivity of the exterior media, the cytoplasm and the membrane, respectively. For the electroporation the parameters are set to $N_0 = 1.5 \times 10^9$, $V_{ep} = 0.258$ V, $q = 2.4606$, $\alpha = 10^9$ m^{-2}s^{-1}, $q_e = 1.68 \times 10^{-19}$ C, $k = 1.38 \times 10^{-23}$ J/K, $T = 310$ K, $\eta = 0.15$, $w_0 = 2.65$ and $\sigma_p = 1.3$ S/m, following [61]. Finally, when dispersive species are accounted for, the parameters are $\tau_e = \tau_c = 9.4 \times 10^{-12}$ s, $\tau_m = 1.1 \times 10^{-7}$ s, and $\epsilon_{c,\infty} = \epsilon_{e,\infty} = 1.2$, and $\epsilon_{m,\infty} = 1.6$.

In order to compare our results to [47] and [61] , we consider a trapezoidal rise-time pulsed voltage waveform of 10 ns over a 20 ns total time. The rise time is set at 2 ns. This later is pictured in Figure 12. Two tests are performed with the same input nsPEF, first, no dispersive species are considered, and second dispersive species in each media are accounted for. The time step for both scenarios is the same and set at $\Delta t = 5 \times 10^{-11}$ for convergence.

Following [47] and [61], for the dispersive species, the rise of the trans-membrane voltage should be faster and if should decrease below 0 after the input pulsed electric field. In both cases, we expect the trans-membrane voltage U_m to increase with the nsPEF until a limit value of around 1.5 V, where the conductivity of the membrane would have increased and be above the conductivity of the exterior media and the cytoplasm. From this point, U_m should decrease. For the density of pores, these parameters should normally increase rapidly until an asymptote at around 10^{16} for

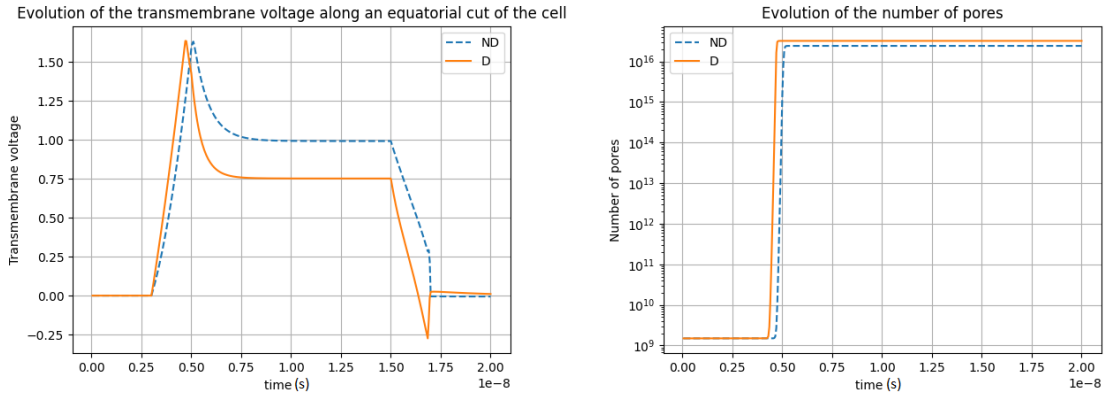

(a) Trans-membrane voltage U_m.

(b) Pore density N

Figure 13: Time response of both the trans-membrane voltage in (a) and of the pore density in (b) when a 10 ns trapezoidal nsPEF is applied for the non-dispersive and dispersive models.

the parameters we have. In Figures 13 (a) and (b), we plot the trans-membrane voltage and the density of pores, respectively. In both figures, the case without dispersive species is in dotted line, while the scenario with dispersive species is in plain line.

We first focus on the trans-membrane voltage pictured in Figure 13. In both cases, this latter is increasing with the pulsed electric field until a limit value of $U_m \simeq 1.5$ V, as expected. Then, the field is rapidly decreasing until 1 V or 0.75 V for the non-dispersive and dispersive models, respectively. Finally, U_m decreases with the nsPEF, and when dispersive species are accounted for U_m decreases below 0. One should also note that the trans-membrane voltage increase is faster with the dispersive model, as in [47]. These results are in line with the one obtained in [61]. Second, the density of pores is increasing with the nsPEF until an asymptote above 10^{16} for both models. This value corresponds to the one obtained in [47, 48, 61].

5. Conclusion

In this work, we have derived a DDFV scheme to solve the Poisson equation with jump conditions and surface charges. This latter has been applied to model the electroporation after showing a second-order convergence on canonical tests.

First, after describing the studied model, a computational based on finite volume has been introduced. This latter is based on a primal/dual mesh leading to better accuracy than usual finite volume methods. Besides, jump conditions as transitions between media are easily taken into account. Thus, the method has been adapted to take into account the jump condition with surface charges of the model. Finally, the linear system that needs to be solved has been obtained. This latter is highly parallelizable and solved using a bi-conjugate gradient method. In addition, a result on the positive definition of the obtained matrix has been shown.

Second, the method has been validated on several canonical tests. Firstly, a two-layered capacitor has been studied in order to exhibit the expected second-order convergence of the method in this case, even with a very distorted mesh. Besides, the error in both L^2 and L^∞ norm is very low. Secondly, we considered surface charges in-between the two layers of dielectric, and obtained a second-order convergence even on a randomly distorted mesh, although the error in L^2-norm was higher.

Finally, the method has been applied to model electroporation. First, a physical model for this phenomenon based on the metal-dielectric equivalence, and Debye model has been obtained. We treated the membrane as a domain, rather than only as an interface, which led to a Poisson equation with jump conditions that could be solved using our DDFV framework. Thus, results have been obtained and compared to the literature in both the stationary case and when the cell is exposed to a nsPEF. In those cases, the DDFV primal/dual mesh allows us to directly compute the potential at the inner and outer surface of the membrane without any interpolation.

It should be noted that this computational strategy could also be applied in other domains where a Poisson equation with jump condition needs to be solved, such as cold plasma modeling, hydro-meteors, or electromagnetic compatibility. Future works will focus on both the use of a self-consistent DDFV method for cold plasma modeling and the generalization to 3D.

Acknowledgments

The authors would like to thank Charles Pierre (Université de Pau et des Pays de l'Adour) for fruitful conversation about the DDFV algorithm and its implementation.

References

[1] S. Pancheshnyi, M. Nudnova, A. Starikovskii, Development of a cathode-directed streamer discharge in air at different pressures: experiment and comparison with direct numerical simulation, Physical Review E 71 (1) (2005) 016407.

[2] D. Bessieres, J. Paillol, A. Bourdon, P. Ségur, E. Marode, A new one-dimensional moving mesh method applied to the simulation of streamer discharges, Journal of Physics D: Applied Physics 40 (21) (2007) 6559.

[3] J. Jánskỳ, V. P. Pasko, Modeling of streamer ignition and propagation in the system of two approaching hydrometeors, Journal of Geophysical Research: Atmospheres 125 (6) (2020) e2019JD031337.

[4] V. Pasko, J. Jansky, Monte Carlo modeling of photoionization in air with application to lightning initiation in low thundercloud fields, in: AGU Fall Meeting Abstracts, Vol. 2021, 2021, pp. AE23A–07.

[5] J. C. Weaver, Electroporation theory, Electroporation protocols for microorganisms (1995) 1–26.

[6] N. Y. Babaeva, M. J. Kushner, Intracellular electric fields produced by dielectric barrier discharge treatment of skin, Journal of Physics D: Applied Physics 43 (18) (2010) 185206.

[7] M. Leguebe, A. Silve, L. M. Mir, C. Poignard, Conducting and permeable states of cell membrane submitted to high voltage pulses: mathematical and numerical studies validated by the experiments, Journal of theoretical biology 360 (2014) 83–94.

[8] A. Guittet, C. Poignard, F. Gibou, A Voronoi interface approach to cell aggregate electropermeabilization, Journal of Computational Physics 332 (2017) 143–159.

[9] E. Kantar, F. Mauseth, E. Ildstad, S. Hvidsten, Interfacial breakdown between dielectric surfaces determined by gas discharge, in: 2017 IEEE Conference on Electrical Insulation and Dielectric Phenomenon (CEIDP), IEEE, 2017, pp. 556–559.

[10] E. Kantar, S. Hvidsten, A deterministic breakdown model for dielectric interfaces subjected to tangential electric field, Journal of Physics D: Applied Physics 54 (29) (2021) 295503.

[11] C. Poignard, A. Silve, Différence de potentiel induite par un champ electrique sur la membrane d'une cellule biologique, La Revue 3 E. I (75) (2014) 11–20.

[12] F. Guo, K. Qian, L. Zhang, X. Liu, H. Peng, Multiphysics modelling of electroporation under uni-or bipolar nanosecond pulse sequences, Bioelectrochemistry 141 (2021) 107878.

[13] M. Leguèbe, C. Poignard, L. Weynans, A second-order cartesian method for the simulation of electropermeabilization cell models, Journal of Computational Physics 292 (2015) 114–140.

[14] O. C. Zienkiewicz, P. Morice, The finite element method in engineering science, Vol. 1977, McGraw-hill London, 1971.

[15] D. Y. Kwak, S. Lee, Y. Hyon, A new finite element for interface problems having robin type jump, International Journal of Numerical Analysis & Modeling 14 (4-5) (2017) 532–549.

[16] R. Eymard, T. Gallouët, R. Herbin, Finite volume methods, Handbook of numerical analysis 7 (2000) 713–1018.

[17] F. Boyer, F. Hubert, Finite Volume Method for 2D Linear and Nonlinear Elliptic Problems with Discontinuities, SIAM Journal on Numerical Analysis 46 (6) (2008) 3032–3070. doi:10.1137/060666196.
URL http://epubs.siam.org/doi/10.1137/060666196

[18] Y. Coudiere, C. Pierre, O. Rousseau, R. Turpault, A 2D/3D Discrete Duality Finite Volume Scheme. Application to ECG simulation, International Journal on Finite Volumes 6 (1) (2008) 1–24.
URL https://hal.archives-ouvertes.fr/hal-00328251/

[19] J. Droniou, Finite volume schemes for diffusion equations: Introduction to and review of modern methods, Mathematical Models and Methods in Applied Sciences 24 (08) (2014) 1575–1619. doi:10.1142/S0218202514400041.
URL https://www.worldscientific.com/doi/abs/10.1142/S0218202514400041

[20] G. Yuan, Z. Sheng, Analysis of accuracy of a finite volume scheme for diffusion equations on distorted meshes, Journal of Computational Physics 224 (2) (2007) 1170–1189. doi:10.1016/j.jcp.2006.11.011.
URL https://www.sciencedirect.com/science/article/pii/S0021999106005717

[21] F. Hermeline, A Finite Volume Method for the Approximation of Diffusion Operators on Distorted Meshes, Journal of Computational Physics 160 (2) (2000) 481–499. doi:10.1006/jcph.2000.6466.
URL https://www.sciencedirect.com/science/article/pii/S0021999100964660

[22] S. Krell, Stabilized DDFV schemes for stokes problem with variable viscosity on general 2D meshes, Numerical Methods for Partial Differential Equations 27 (6) (2011) 1666–1706, publisher: John Wiley & Sons, Ltd. doi:10.1002/num.20603.
URL https://doi.org/10.1002/num.20603

[23] F. Hermeline, Approximation of diffusion operators with discontinuous tensor coefficients on distorted meshes, Computer methods in applied mechanics and engineering 192 (16-18) (2003) 1939–1959.

[24] Y. Coudiere, F. Hubert, G. Manzini, A CeVeFE DDFV scheme for discontinuous anisotropic permeability tensors, in: Finite Volumes for Complex Applications VI Problems & Perspectives, Springer, 2011, pp. 283–291.

[25] J. M. Hyman, S. Li, P. Knupp, M. Shashkov, An algorithm for aligning a quadrilateral grid with internal boundaries, Journal of Computational Physics 163 (1) (2000) 133–149.

[26] Y. Coudière, C. Pierre, R. Turpault, A 2d/3d finite volume method used to solve the bidomain equations of electrocardiology, in: Algorithmy 2009, 2009, pp. 1–10.

[27] J. W. Barrett, C. M. Elliott, Finite element approximation of the Dirichlet problem using the boundary penalty method, Numerische Mathematik 49 (4) (1986) 343–366. doi:10.1007/BF01389536.
URL https://doi.org/10.1007/BF01389536

[28] B. Maury, Numerical Analysis of a Finite Element/Volume Penalty Method, SIAM Journal on Numerical Analysis 47 (2) (2009) 1126–1148. doi:10.1137/080712799.
URL http://epubs.siam.org/doi/10.1137/080712799

[29] C. Pierre, Modélisation et simulation de l'activité électrique du coeur dans le thorax, analyse numérique et méthodes de volumes finis, Ph.D. thesis, Université de Nantes (2005).

[30] V. E. Henson, U. M. Yang, BoomerAMG: A parallel algebraic multigrid solver and preconditioner, Developments and Trends in Iterative Methods for Large Systems of Equations - in memorium Rudiger Weiss 41 (1) (2002) 155–177. doi:10.1016/S0168-9274(01)00115-5.
URL https://www.sciencedirect.com/science/article/pii/S0168927401001155

[31] R. D. Falgout, J. E. Jones, U. M. Yang, The Design and Implementation of hypre, a Library of Parallel High Performance Preconditioners, in: A. M. Bruaset, A. Tveito (Eds.), Numerical Solution of Partial Differential Equations on Parallel Computers, Springer Berlin Heidelberg, Berlin, Heidelberg, 2006, pp. 267–294.

[32] J. Hyman, M. Shashkov, S. Steinberg, The Numerical Solution of Diffusion Problems in Strongly Heterogeneous Non-isotropic Materials, Journal of Computational Physics 132 (1) (1997) 130–148. doi:10.1006/jcph.1996.5633.
URL https://www.sciencedirect.com/science/article/pii/S0021999196956338

[33] F. Lohr, D. Y. Lo, D. A. Zaharoff, K. Hu, X. Zhang, Y. Li, Y. Zhao, M. W. Dewhirst, F. Yuan, C.-Y. Li, Effective tumor therapy with plasmid-encoded cytokines combined with in vivo electroporation, Cancer research 61 (8) (2001) 3281–3284.

[34] A. Gothelf, L. M. Mir, J. Gehl, Electrochemotherapy: results of cancer treatment using enhanced delivery of bleomycin by electroporation, Cancer treatment reviews 29 (5) (2003) 371–387.

[35] H. Potter, Electroporation in biology: methods, applications, and instrumentation, Analytical biochemistry 174 (2) (1988) 361–373.

[36] F. Andre, L. Mir, DNA electrotransfer: its principles and an updated review of its therapeutic applications, Gene therapy 11 (1) (2004) S33–S42.

[37] A. I. Daud, R. C. DeConti, S. Andrews, P. Urbas, A. I. Riker, V. K. Sondak, P. N. Munster, D. M. Sullivan, K. E. Ugen, J. L. Messina, et al., Phase I trial of interleukin-12 plasmid electroporation in patients with metastatic melanoma, Journal of clinical oncology 26 (36) (2008) 5896.

[38] M. Zeira, P.-F. Tosi, Y. Mouneimne, J. Lazarte, L. Sneed, D. J. Volsky, C. Nicolau, Full-length CD4 electroinserted in the erythrocyte membrane as a long-lived inhibitor of infection by human immunodeficiency virus., Proceedings of the National Academy of Sciences 88 (10) (1991) 4409–4413.

[39] P. T. Vernier, Y. Sun, L. Marcu, S. Salemi, C. M. Craft, M. A. Gundersen, Calcium bursts induced by nanosecond electric pulses, Biochemical and biophysical research communications 310 (2) (2003) 286–295.

[40] K. C. Smith, J. C. Weaver, Active mechanisms are needed to describe cell responses to submicrosecond, megavolt-per-meter pulses: cell models for ultrashort pulses, Biophysical journal 95 (4) (2008) 1547–1563.

[41] J. Teissie, Electropermeabilization of the cell membrane, Electroporation Protocols (2014) 25–46.

[42] T. R. Gowrishankar, A. T. Esser, Z. Vasilkoski, K. C. Smith, J. C. Weaver, Microdosimetry for conventional and supra-electroporation in cells with organelles, Biochemical and biophysical research communications 341 (4) (2006) 1266–1276.

[43] T. Kotnik, D. Miklavčič, Analytical description of transmembrane voltage induced by electric fields on spheroidal cells, Biophysical Journal 79 (2) (2000) 670–679.

[44] Q. Hu, R. Joshi, Transmembrane voltage analyses in spheroidal cells in response to an intense ultrashort electrical pulse, Physical Review E 79 (1) (2009) 011901.

[45] O. Kavian, M. Leguèbe, C. Poignard, L. Weynans, "Classical" electropermeabilization modeling at the cell scale, Journal of mathematical biology 68 (2014) 235–265.

[46] B. Deka, P. Roy, Weak Galerkin finite element methods for electric interface model with nonhomogeneous jump conditions, Numerical Methods for Partial Differential Equations 36 (4) (2020) 734–755.

[47] E. Salimi, D. J. Thomson, G. E. Bridges, Membrane dielectric dispersion in nanosecond pulsed electroporation of biological cells, IEEE Transactions on Dielectrics and Electrical Insulation 20 (4) (2013) 1256–1265.

[48] F. Guo, L. Zhang, X. Liu, Nonlinear dispersive cell model for microdosimetry of nanosecond pulsed electric fields, Scientific Reports 10 (1) (2020) 1–11.

[49] D. Ghosh, N. K. Saluja, T. G. Singh, A FEM study of molecular transport through a single nanopore in a spherical cell, Biointerface Research in Applied Chemistry 12 (3) (2022) 2958–2969.

[50] T. Kotnik, D. Miklavčič, Theoretical evaluation of voltage inducement on internal membranes of biological cells exposed to electric fields, Biophysical journal 90 (2) (2006) 480–491.

[51] Z. Vasilkoski, A. T. Esser, T. Gowrishankar, J. C. Weaver, Membrane electroporation: The absolute rate equation and nanosecond time scale pore creation, Physical review E 74 (2) (2006) 021904.

[52] C. Yao, Y. Mi, C. Li, X. Hu, X. Chen, C. Sun, Study of transmembrane potentials on cellular inner and outer membrane—frequency response model and its filter characteristic simulation, IEEE Transactions on Biomedical Engineering 55 (7) (2008) 1792–1799.

[53] C. Merla, A. Denzi, A. Paffi, M. Casciola, G. d'Inzeo, F. Apollonio, M. Liberti, Novel passive element circuits for microdosimetry of nanosecond pulsed electric fields, IEEE Transactions on Biomedical Engineering 59 (8) (2012) 2302–2311.

[54] T. D. T. Vu, S. Kohler, C. Merla, D. Arnaud-Cormos, P. Leveque, FDTD-based microdosimetry for high-intensity nanosecond pulsed electric fields (nsPEFs) application, in: 2012 IEEE/MTT-S International Microwave Symposium Digest, IEEE, 2012, pp. 1–3.

[55] E. Salimi, G. Bridges, D. Thomson, The effect of dielectric relaxation in nanosecond pulse electroporation of biological cells, in: 2010 14th International Symposium on Antenna Technology and Applied Electromagnetics & the American Electromagnetics Conference, IEEE, 2010, pp. 1–4.

[56] T. D. T. Vu, Contribution à la modélisation du comportement électromagnétique de milieux biologiques exposés à des impulsions de champ électrique nanosecondes, Ph.D. thesis, Limoges (2012).

[57] C. Böttcher, O. Van Belle, P. Bordewijk, A. Rip, D. D. Yue, Theory of electric polarization, Journal of The Electrochemical Society 121 (6) (1974) 211C.

[58] S. Gabriel, R. Lau, C. Gabriel, The dielectric properties of biological tissues: III. Parametric models for the dielectric spectrum of tissues, Physics in medicine & biology 41 (11) (1996) 2271.

[59] G. Pucihar, D. Miklavcic, T. Kotnik, A time-dependent numerical model of transmembrane voltage inducement and electroporation of irregularly shaped cells, IEEE Transactions on Biomedical Engineering 56 (5) (2009) 1491–1501.

[60] R. P. Joshi, Q. Hu, K. H. Schoenbach, Modeling studies of cell response to ultrashort, high-intensity electric fields-implications for intracellular manipulation, IEEE Transactions on Plasma Science 32 (4) (2004) 1677–1686.

[61] F. Guo, K. Qian, L. Zhang, H. Deng, X. Li, J. Zhou, J. Wang, Anisotropic conductivity for single-cell electroporation simulation with tangentially dispersive membrane, Electrochimica Acta 385 (2021) 138426.